MicroRNA-188 regulates age-related switch between osteoblast and adipocyte differentiation

Chang-Jun Li,[1,2] Peng Cheng,[1,3] Meng-Ke Liang,[1] Yu-Si Chen,[1] Qiong Lu,[1] Jin-Yu Wang,[1] Zhu-Ying Xia,[1] Hou-De Zhou,[1] Xu Cao,[2] Hui Xie,[1] Er-Yuan Liao,[1] and Xiang-Hang Luo[1]

[1]Institute of Endocrinology and Metabolism, The Second Xiangya Hospital of Central South University, Changsha, Hunan, China. [2]Department of Orthopaedic Surgery, Johns Hopkins University School of Medicine, Baltimore, Maryland, USA. [3]Department of Gerontology, The First Hospital Affiliated to Nanjing Medical University, Nanjing, Jiangsu, China.

Bone marrow mesenchymal stem cells (BMSCs) exhibit an age-dependent reduction in osteogenesis that is accompanied by an increased propensity toward adipocyte differentiation. This switch increases adipocyte numbers and decreases the number of osteoblasts, contributing to age-related bone loss. Here, we found that the level of microRNA-188 (miR-188) is markedly higher in BMSCs from aged compared with young mice and humans. Compared with control mice, animals lacking miR-188 showed a substantial reduction of age-associated bone loss and fat accumulation in bone marrow. Conversely, mice with transgenic overexpression of miR-188 in osterix$^+$ osteoprogenitors had greater age-associated bone loss and fat accumulation in bone marrow relative to WT mice. Moreover, using an aptamer delivery system, we found that BMSC-specific overexpression of miR-188 in mice reduced bone formation and increased bone marrow fat accumulation. We identified histone deacetylase 9 (HDAC9) and RPTOR-independent companion of MTOR complex 2 (RICTOR) as the direct targets of miR-188. Notably, BMSC-specific inhibition of miR-188 by intra–bone marrow injection of aptamer-antagomiR-188 increased bone formation and decreased bone marrow fat accumulation in aged mice. Together, our results indicate that miR-188 is a key regulator of the age-related switch between osteogenesis and adipogenesis of BMSCs and may represent a potential therapeutic target for age-related bone loss.

Introduction

Bone marrow mesenchymal stem cells (BMSCs) have the potential to differentiate into various cell types, including adipocytes, chondrocytes, and osteoblasts (1, 2). Age-related osteoporosis is characterized by reduced bone formation and increased marrow fat accumulation (3–6). This age-related reduction in osteoblast activity is partly caused by the fact that BMSCs from elderly subjects have reduced capacity to differentiate into osteoblasts and increased capacity to differentiate into adipocytes (3, 4). However, the molecular mechanisms behind the shift from osteoblast to adipocyte differentiation in BMSCs remain elusive.

MicroRNAs (miRNAs) are a class of small (~22 nucleotides), single-stranded noncoding RNAs found in diverse organisms, which downregulate the expression of target genes by either mRNA degradation or translational inhibition (6, 7). Recently, several miRNAs were found to be involved in either osteogenesis or adipogenesis (8–12). However, most of these miRNAs have only been investigated in vitro, and their functional roles in the pathophysiological mechanisms responsible for age-related bone loss and accumulation of fat in bone marrow remain to be established. The roles of miRNAs in the age-related switch between osteoblast and adipocyte differentiation of BMSCs in bone marrow are also unclear.

Here, we identified a novel, highly expressed miRNA, miR-188, from the BMSCs of aged mice and human subjects. Our study demonstrated that miR-188 regulates BMSCs' bifurcation into osteoblasts and adipocytes during aging. Knockout of *Mir188* in mice reduced age-associated trabecular and cortical bone loss and marrow fat accumulation. Notably, intra–bone marrow injection of BMSC-targeting aptamer-antagomiR-188 stimulated trabecular and cortical-endosteal bone formation and decreased bone marrow fat accumulation in aged mice. Thus, our study provides a new mechanism and a novel therapeutic target for age-related bone loss.

Results

Aging induces miR-188 expression in BMSCs. Histological and immunohistochemical analyses of femora revealed increased number and area of adipocytes characterized by fat vacuoles in bone marrow and decreased number of osteocalcin-positive osteoblasts on the trabecular and endosteal bone surfaces in aged mice (18 months old) compared with young mice (3 months old) (Figure 1, A–D, and Supplemental Figure 1; supplemental material available online with this article; doi:10.1172/JCI77716DS1). The increased bone marrow fat accumulation and decreased osteoblasts implied a switch from osteogenic differentiation to adipogenic differentiation of BMSCs. To determine the mechanism of the age-related differentiation switch of BMSCs, Sca-1$^+$CD29$^+$CD45$^-$CD11b$^-$ mesenchymal stem cells were sorted by FACS from bone marrow cells (13) of young and aged mice to identify dysregulated miRNAs by performing miRNA microarray analysis (Figure 1E). Among them, miR-188 showed the largest difference in expression between the 2 groups, being expressed approximately 30 times more highly in aged mice compared with young mice. The raw data of the microarray have been uploaded to GEO with the series record GSE57127 (http://www.ncbi.nlm.nih.gov/geo/query/acc.cgi?acc=GSE57127).

Conflict of interest: The authors have declared that no conflict of interest exists.
Submitted: June 27, 2014; **Accepted:** January 15, 2015.
Reference information: *J Clin Invest*. 2015;125(4):1509–1522. doi:10.1172/JCI77716.

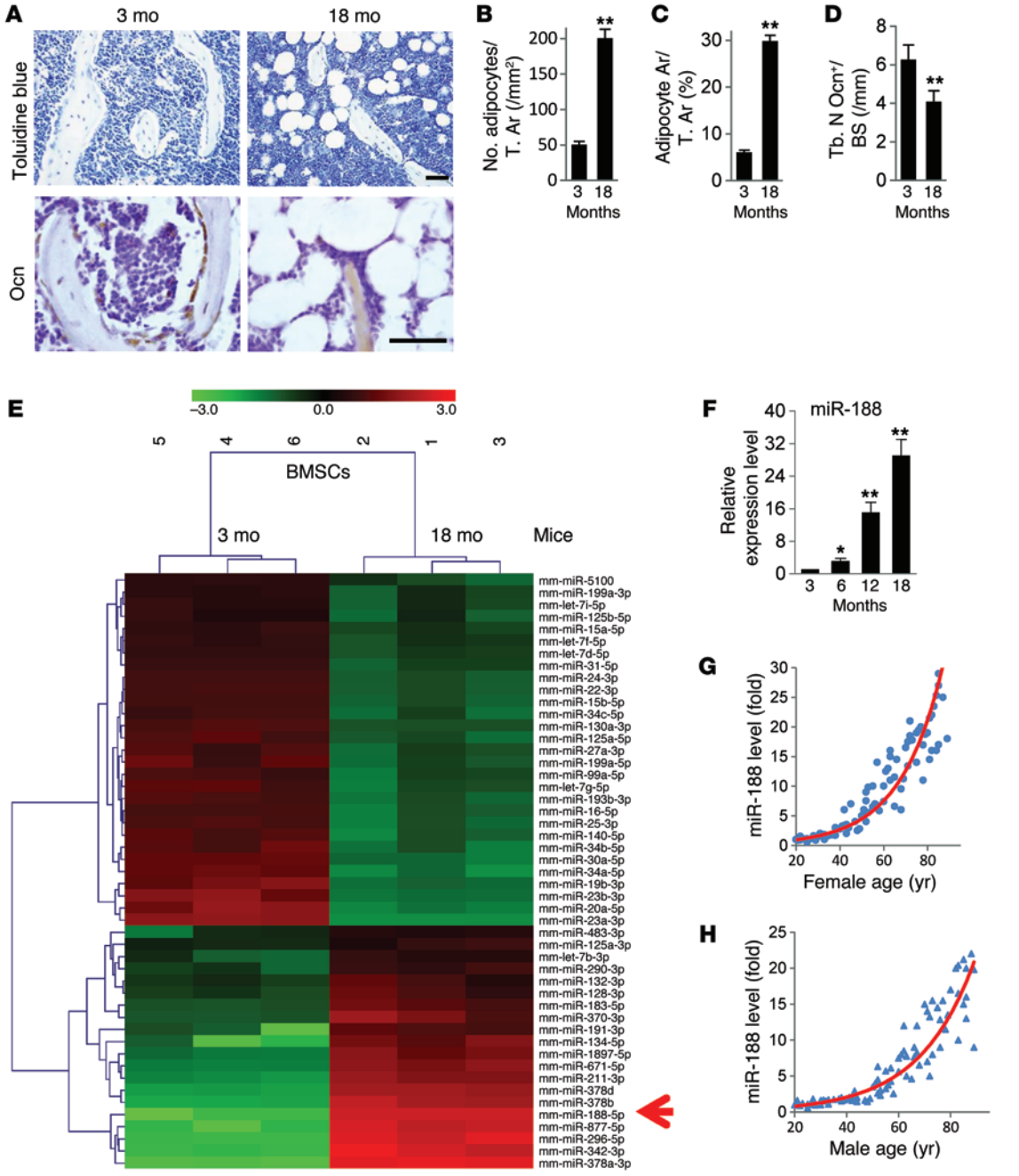

Figure 1. Aging induces miR-188 expression in BMSCs. (**A**–**D**) Representative images of toluidine blue (T.) staining (**A**, top) and osteocalcin (Ocn) immunohistochemical staining (**A**, bottom) and quantification of number and area (Ar) of adipocytes (**B** and **C**) and number of osteoblasts (**D**) in distal femora from 3-month-old and 18-month-old female C57BL/6 mice. Tb. N, trabecular number. Scale bars: 100 μm. *n* = 6 per group. (**E**) Microarray profiling results of deregulated miRNAs in BMSCs from young and aged mice. (**F**) qRT-PCR analysis of the levels of miR-188 expression in BMSCs derived from the mice at different ages. *n* = 6 per group. (**G** and **H**) Age-associated changes of miR-188 levels in BMSCs from 85 human females (**G**) and 85 males (**H**). Data shown as mean ± SD. **P* < 0.05, ***P* < 0.01 (**B**–**D**, Student's *t* test; **F**, ANOVA).

The increased level of miR-188 was further confirmed by quantitative real-time RT-PCR (qRT-PCR) (Figure 1F).

We then isolated human BMSCs (defined as positive for STRO-1 and CD146 and negative for CD45) (14) from bone marrow cells by FACS. Notably, the miR-188 level in human BMSCs was positively correlated with age (Figure 1, G and H). These data suggest that miR-188 plays an important role in the aging process of BMSCs in both mouse and human.

MiR-188 knockout mice show reduced age-associated bone loss and marrow fat accumulation. To investigate the role of miR-188 in vivo, we generated mir-188 knockout (*Mir188*$^{-/-}$) mice via gene targeting mediated by transcription activator–like effector nuclease (TALEN) (Supplemental Figure 2, A and B, and ref. 15). The trabecular bone volume and number were higher and the trabecular separation was lower in the femora of aged (12 or 18 months old) *Mir188*$^{-/-}$ mice relative to their WT littermates (Figure 2, A–E).

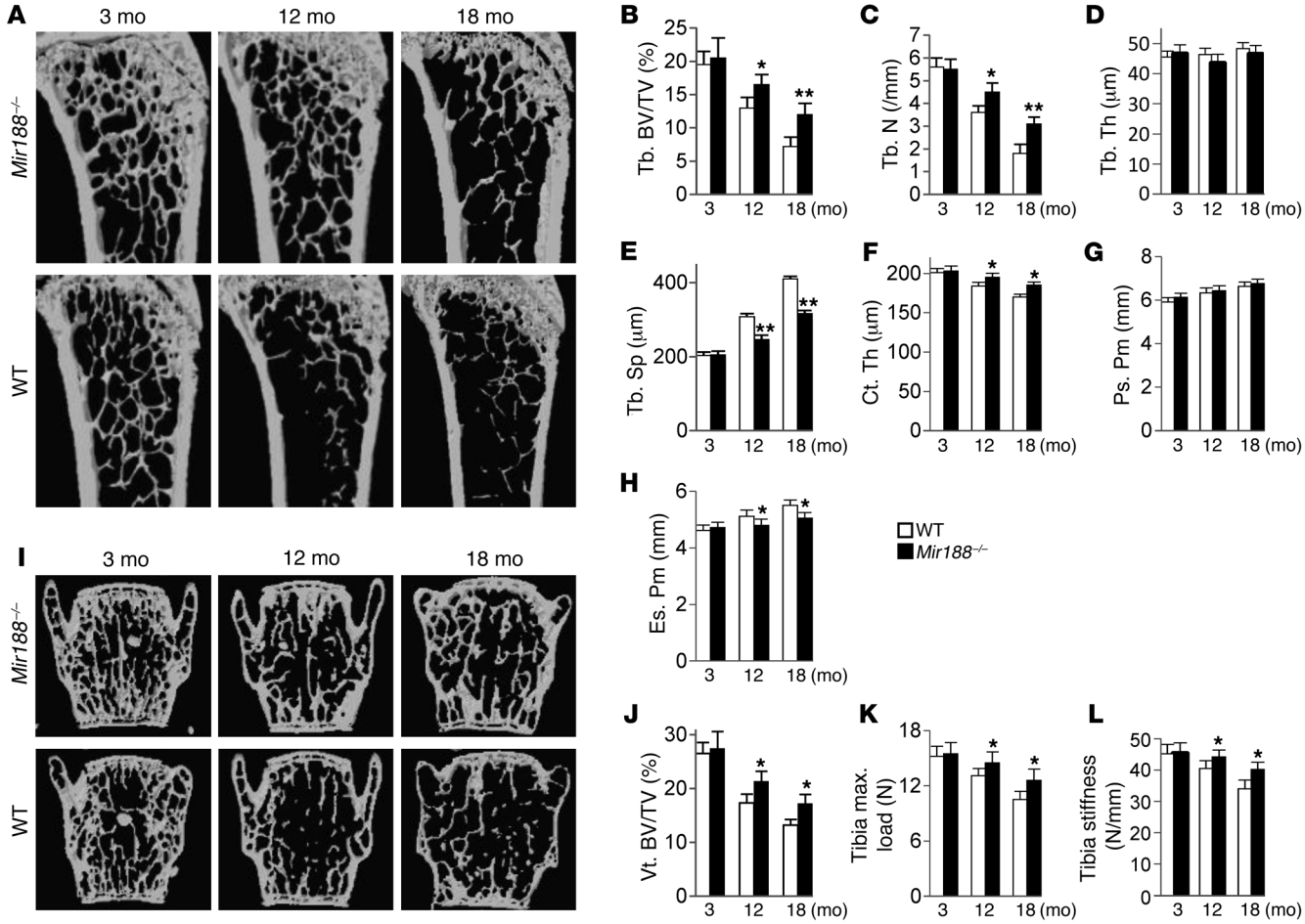

Figure 2. *Mir188*$^{-/-}$ mice exhibit reduced age-associated bone loss. (**A**–**H**) Representative microcomputed tomography (μCT) images (**A**) and quantitative μCT analysis of trabecular (**B**–**E**) and cortical (**F**–**H**) bone microarchitecture in femora from 3-, 12-, and 18-month-old WT and miR-188 knockout (*Mir188*$^{-/-}$) mice. *n* = 6 per group. Tb. BV/TV, trabecular bone volume per tissue volume; Tb. Th, trabecular thickness; Tb. Sp, trabecular separation; Ct. Th, cortical thickness; Ps. Pm, periosteal perimeter; Es. Pm, endosteal perimeter. (**I** and **J**) Representative μCT images (**I**) and quantification of the ratio of bone volume to tissue volume (**J**) of L4 vertebrae (Vt. BV/TV). *n* = 6 per group. (**K** and **L**) Three-point bending measurement of tibia maximum load (**K**) and stiffness (**L**). *n* = 5 per group. Data shown as mean ± SD. **P* < 0.05, ***P* < 0.01 (Student's *t* test).

The cortical bone thickness was higher and the endosteal perimeter was lower in the femora of aged *Mir188*$^{-/-}$ mice compared with their WT littermates (Figure 2, F–H). The vertebral bone volume was also higher in aged *Mir188*$^{-/-}$ mice compared with their WT littermates (Figure 2, I and J). Accordingly, values of the tibia maximum load and stiffness, which represent bone strength, were higher in the aged *Mir188*$^{-/-}$ mice than in their WT littermates (Figure 2, K and L). Calcein double labeling confirmed that aged *Mir188*$^{-/-}$ mice had significantly higher trabecular and endosteal bone formation rates (BFRs) compared with their WT littermates (Figure 3, A–D). However, no significant differences were observed between the young (3 months old) *Mir188*$^{-/-}$ mice and their WT littermates (Figure 2 and Figure 3, A–I).

Aged, but not young, *Mir188*$^{-/-}$ mice had significantly decreased number and area of adipocytes in the bone marrow (Figure 3, E–G) and higher number and surface of osteoblasts on the trabecular and endosteal bone surfaces (Figure 3, H and I, and Supplemental Figure 3, A and B) compared with their WT littermates. The number and surface of osteoclasts on the trabecular bone surface were not changed in *Mir188*$^{-/-}$ mice relative to their WT littermates (Supplemental Figure 3B). In vitro, BMSCs from *Mir188*$^{-/-}$ mice exhibited increased osteogenesis and decreased adipogenesis (Figure 3J). However, culture of bone marrow monocytes/macrophages showed that osteoclast formation was not affected (Supplemental Figure 3C).

Taken together, the results suggest that *Mir188*$^{-/-}$ mice have reduced age-associated bone loss and marrow fat accumulation.

Transgenic expression of miR-188 in osterix^{+} *osteoprogenitors leads to an accelerated bone marrow fat accumulation and bone loss.* We then constructed transgenic mice overexpressing miR-188 in osterix^{+} osteoprogenitors to investigate whether overexpression of miR-188 in vivo would lead to bone loss and marrow fat accumulation. qRT-PCR revealed significantly higher levels of miR-188 expression in both line 1 and line 2 as compared with that in WT controls (Supplemental Figure 4A). Both line 1 and line 2 (6 months of age) had lower trabecular bone volume of femur and vertebra relative to WT controls (Figure 4, A–E and I, and Supplemental Figure 4B). We chose the line 1 mice with higher miR88 expression (referred to as "transgenic mice" hereafter) for detailed analysis.

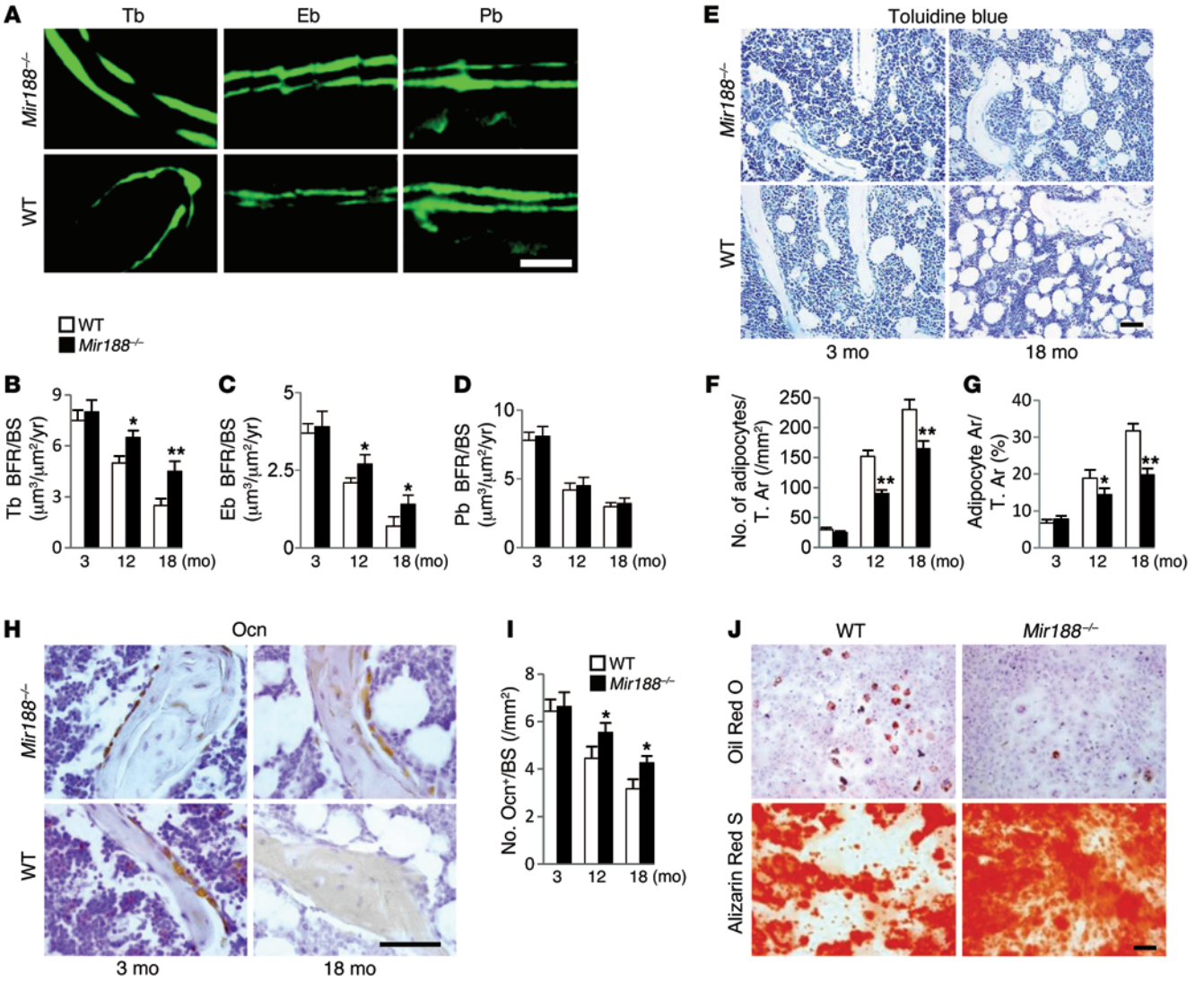

Figure 3. *Mir188*$^{-/-}$ mice show higher osteoblastic bone formation and lower marrow fat accumulation in aged mice. (**A**) Representative images of calcein double labeling of trabecular (Tb), endosteal (Eb), and periosteal bone (Pb) with quantification (**B**–**D**) of bone formation rate per bone surface (BFR/BS) in femora of 18-month-old WT and *Mir188*$^{-/-}$ mice. Scale bar: 50 μm. $n = 6$ per group. (**E**) Representative images of toluidine blue staining with quantification of number and area of adipocytes in distal femora (**F** and **G**). Scale bar: 100 μm. (**H**) Representative images of osteocalcin immunohistochemical staining with quantification of number of osteoblasts in distal femora (**I**). Scale bar: 100 μm. $n = 6$ per group. (**J**) Representative images of Oil Red O staining of lipids (top) and Alizarin Red S staining of matrix mineralization (bottom) in BMSCs from *Mir188*$^{-/-}$ mice and WT mice cultured in adipogenesis induction medium for 14 days and osteogenesis induction medium for 21 days, respectively. Scale bar: 100 μm. Data are representative of 3 independent experiments. Data shown as mean ± SD. $^{*}P < 0.05$, $^{**}P < 0.01$ (Student's *t* test).

The trabecular bone volume, number, and cortical bone thickness were lower, and the trabecular separation and endosteal perimeter were higher, in the femora of 6-month-old and 12-month-old transgenic mice relative to WT controls (Figure 4, A–H). The vertebral bone volume was also lower in miR-188 transgenic mice relative to WT controls (Figure 4I). In addition, bone strength was lower in the miR-188 transgenic mice compared with WT controls (Figure 4, J and K). MiR-188 transgenic mice had significantly lower trabecular and endosteal BFRs relative to WT controls (Figure 4, L–N). Moreover, miR-188 transgenic mice had significantly higher number and area of adipocytes in the bone marrow and lower number and surface of osteoblasts on the trabecular and endosteal bone surfaces as compared with WT controls (Figure 4, O–R, and Supplemental Figure 5, A and B). However, no differences of the osteoclast number and surface were observed between miR-188 transgenic mice and their WT controls (Supplemental Figure 5B).

Thus, these data confirm that overexpressing miR-188 in osterix^{+} osteoprogenitors of transgenic mice leads to bone loss and an accelerated formation of fatty marrow.

Mice with BMSC-specific overexpression of miR-188 using aptamer delivery system present reduced bone formation and increased bone marrow fat. To investigate the effects of miR-188 overexpression in BMSCs of mice, agomiR-188 was injected into the bone marrow with a BMSC-targeting aptamer, which can specifically bind to BMSCs (16–18). We tested the ability of the aptamer to bind to mouse BMSCs, monocytes/macrophages, and preosteoclasts.

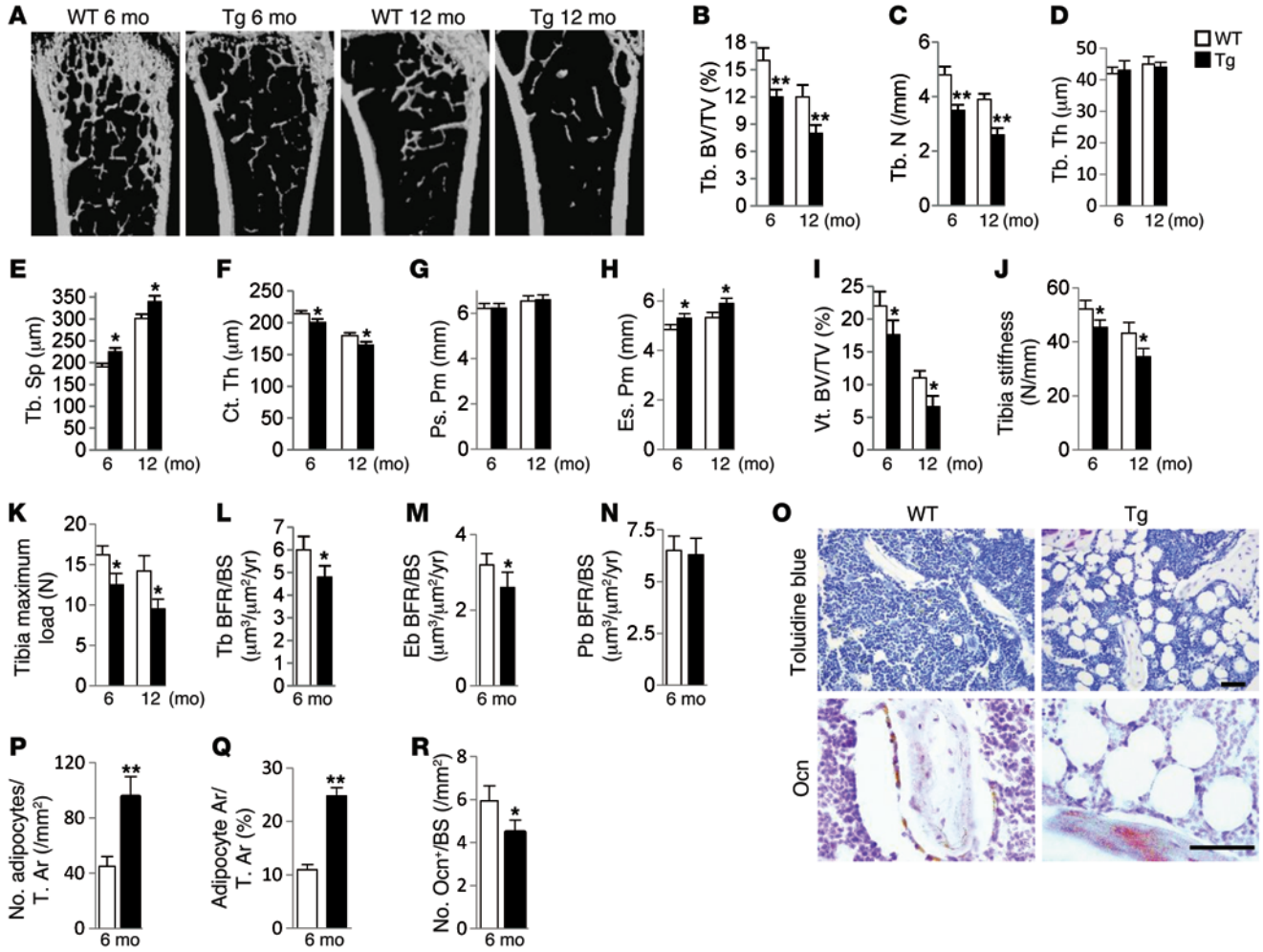

Figure 4. Mice with transgenic overexpression of miR-188 in osterix⁺ osteoprogenitors exhibit accelerated bone marrow fat accumulation and bone loss. (**A**) Representative μCT images with quantitative μCT analysis of trabecular and cortical bone microarchitecture (**B**–**H**) in femora from 6- and 12-month-old WT and miR-188 transgenic (Tg) mice. *n* = 6 per group. (**I**) Quantitative μCT analysis of the ratio of bone volume to tissue volume of L4 vertebrae (Vt. BV/TV). (**J** and **K**) Three-point bending measurement of tibia stiffness (**J**) and maximum load (**K**). *n* = 5 per group. (**L**–**N**) Calcein double labeling–based quantification of bone formation rate per bone surface (BFR/BS) in femora. *n* = 5 per group. (**O**–**R**) Representative images of toluidine blue staining (**O**, top) and osteocalcin immunohistochemical staining (**O**, bottom) and quantification of number and area of adipocytes (**P** and **Q**) and number of osteoblasts (**R**) in distal femora. *n* = 8 per group. Data shown as mean ± SD. $^*P < 0.05$, $^{**}P < 0.01$ (Student's *t* test). Scale bar: 100 μm.

FACS analysis showed that binding shift was observed only in BMSCs, not in monocytes/macrophages or preosteoclasts, demonstrating that the selected aptamer had high specificity for BMSCs (Supplemental Figure 6A).

The qRT-PCR results also confirmed that intra–bone marrow injection of aptamer-agomiR-188 caused a significant increase in the level of miR-188 expression in BMSCs, but not in monocytes/macrophages or preosteoclasts (Figure 5A and Supplemental Figure 6B). Mice treated with aptamer-miR-188 showed significantly lower trabecular bone volume, number, and cortical thickness, and higher trabecular separation and endosteal perimeter, compared with vehicle-treated mice (Figure 5, B–I). As a result, bone strength was lower in aptamer-miR-188–treated mice compared with vehicle-treated mice (Figure 5, J and K). Calcein double labeling confirmed that aptamer-miR-188–treated mice had significantly lower trabecular and endosteal BFRs compared with vehicle-treated mice (Figure 5, L–N). Moreover, aptamer-miR-188–treated mice had significantly higher number and area of adipocytes in the bone marrow and lower number and surface of osteoblasts on the trabecular and endosteal bone surfaces (Figure 5, O–R, and Supplemental Figure 6, C and D) as compared with vehicle-treated mice. However, no differences of the osteoclast number and surface were observed between these 2 groups of mice (Supplemental Figure 6D).

These results reveal that mice with BMSC-specific overexpression of miR-188 have reduced bone formation and increased bone marrow fat.

MiR-188 promotes adipogenic differentiation of BMSCs. The qRT-PCR data showed that miR-188 expression increased gradually during adipogenesis of BMSCs (Figure 6A). To investigate the role of miR-188 during adipogenesis, BMSCs were transfected with the agomiR-188 or antagomiR-188 to overexpress or silence miR-188 (Figure 6B). The BMSCs were then cultured in adipogenesis induction medium. Overexpression of miR-188 facilitated lipid droplet formation in BMSCs induced by adipogenesis

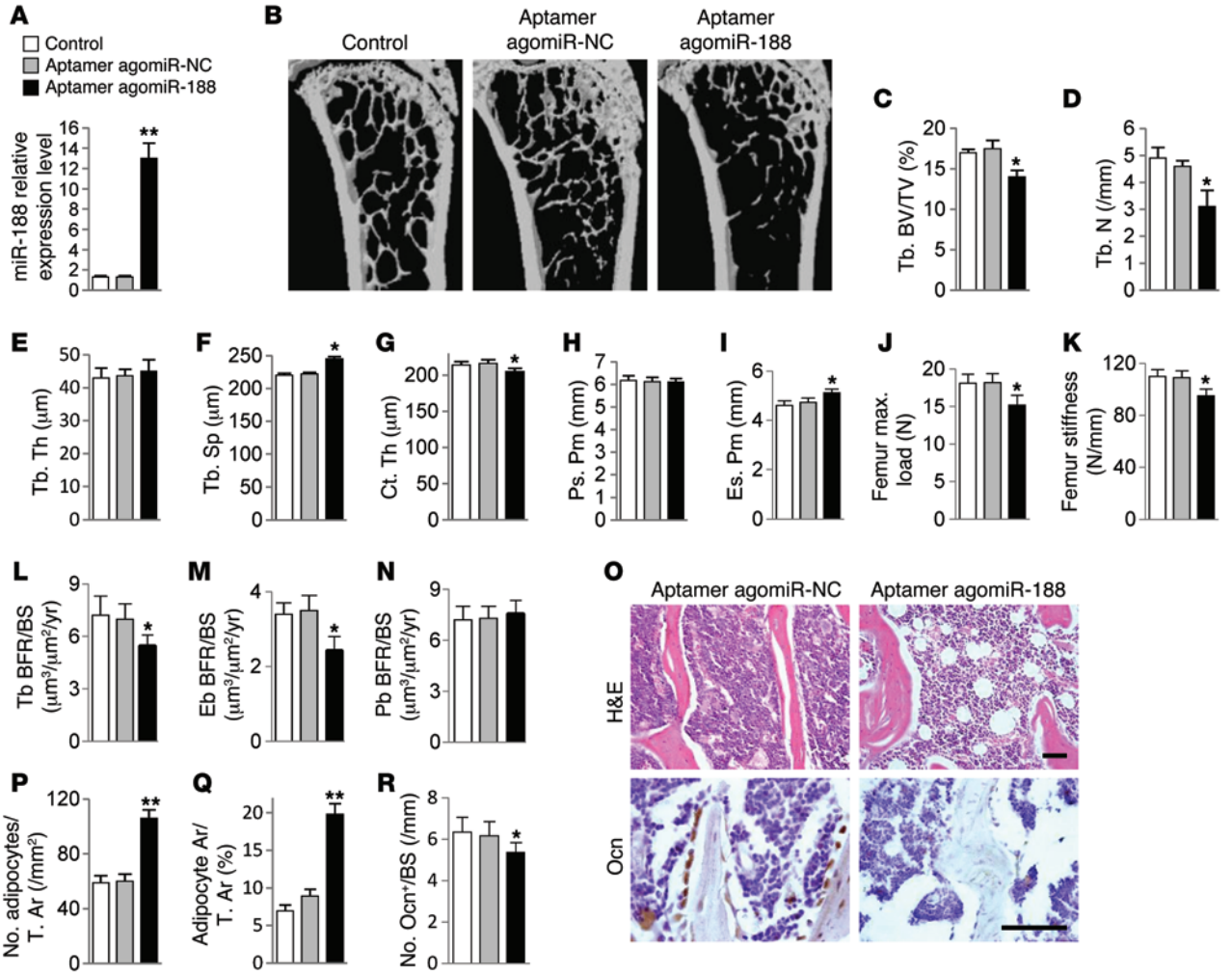

Figure 5. Mice with BMSC-specific overexpression of miR-188 using aptamer delivery system exhibit reduced bone formation and increased marrow fat accumulation. (**A**) qRT-PCR analysis of levels of miR-188 expression in BMSCs of mice with aptamer delivery. NC, negative control. $n = 6$ per group. (**B**–**I**) Representative μCT images (**B**) and quantitative μCT analysis of trabecular (**C**–**F**) and cortical bone (**G**–**I**) microarchitecture in femora from aptamer-treated mice. $n = 10$. (**J** and **K**) Three-point bending measurement of femur maximum load (**J**) and stiffness (**K**). $n = 5$ per group. (**L**–**N**) Calcein double labeling–based quantification of bone formation rate per bone surface (BFR/BS) in femora. $n = 5$ per group. (**O**–**R**) Representative images of H&E staining (**O**, top) and osteocalcin immunohistochemical staining (**O**, bottom) and quantification of number and area of adipocytes (**P** and **Q**) and number of osteoblasts (**R**) in distal femora. Scale bars: 100 μm. $n = 5$ per group. Data shown as mean ± SD. $^*P < 0.05$, $^{**}P < 0.01$ (ANOVA).

induction medium (Figure 6, C and D), accompanied by increased mRNA levels of peroxisome proliferator–activated receptor-g (*Pparg*) and fatty acid binding protein 4 (*Fabp4*), 2 key markers of adipocyte differentiation (Figure 6, E and F). By contrast, silencing of miR-188 attenuated adipogenic differentiation of BMSCs (Figure 6, C and D) and inhibited *Pparg* and *Fabp4* mRNA expression in BMSCs (Figure 6, E and F). The gene microarray analysis further confirmed that mRNA expression levels of *Pparg* and *Fabp4*, as well as other adipocyte differentiation markers (*Igfbp2*, *Lpi*, *Mgst3*), were lower in adipogenic induction medium–induced BMSCs of *Mir188*$^{-/-}$ mice as compared with their WT littermates (Figure 6G). The raw data of the microarray have been uploaded to GEO with the series record GSE63725 (http://www.ncbi.nlm.nih.gov/geo/query/acc.cgi?acc=GSE63725). All of these results suggest that miR-188 promotes adipogenic differentiation of BMSCs.

MiR-188 inhibits osteoblastic differentiation of BMSCs. The expression of miR-188 decreased gradually during osteogenesis, as assessed by qRT-PCR (Figure 7A). To investigate the role of miR-188 during osteoblastic differentiation, BMSCs were transfected with agomiR-188 or antagomiR-188 to overexpress or silence miR-188 and then cultured in osteogenesis induction medium. Overexpression of miR-188 inhibited, while silencing of miR-188 promoted, osteogenic differentiation of BMSCs measured by Alizarin Red staining (Figure 7, B and C).

Consistently, osteoblast differentiation markers, alkaline phosphatase (ALP) activity and osteocalcin secretion, were lower in agomiR-188–transfected cells compared with control cells (Figure 7, D and E). Moreover, the mRNA level of the late-stage second osteoblast transcription factor osterix, but not the first osteoblast transcription factor *Runx2*, was inhibited by agomiR-188 (Figure 7, F and G). Conversely, antagomiR-188 transfection promoted osteogenic differentiation and increased osterix expression (Figure 7, B–G). Moreover, gene microarray analysis further confirmed that *Alpl* (ALP), *Col1a* (collagen type I α), *Sp7* (osterix),

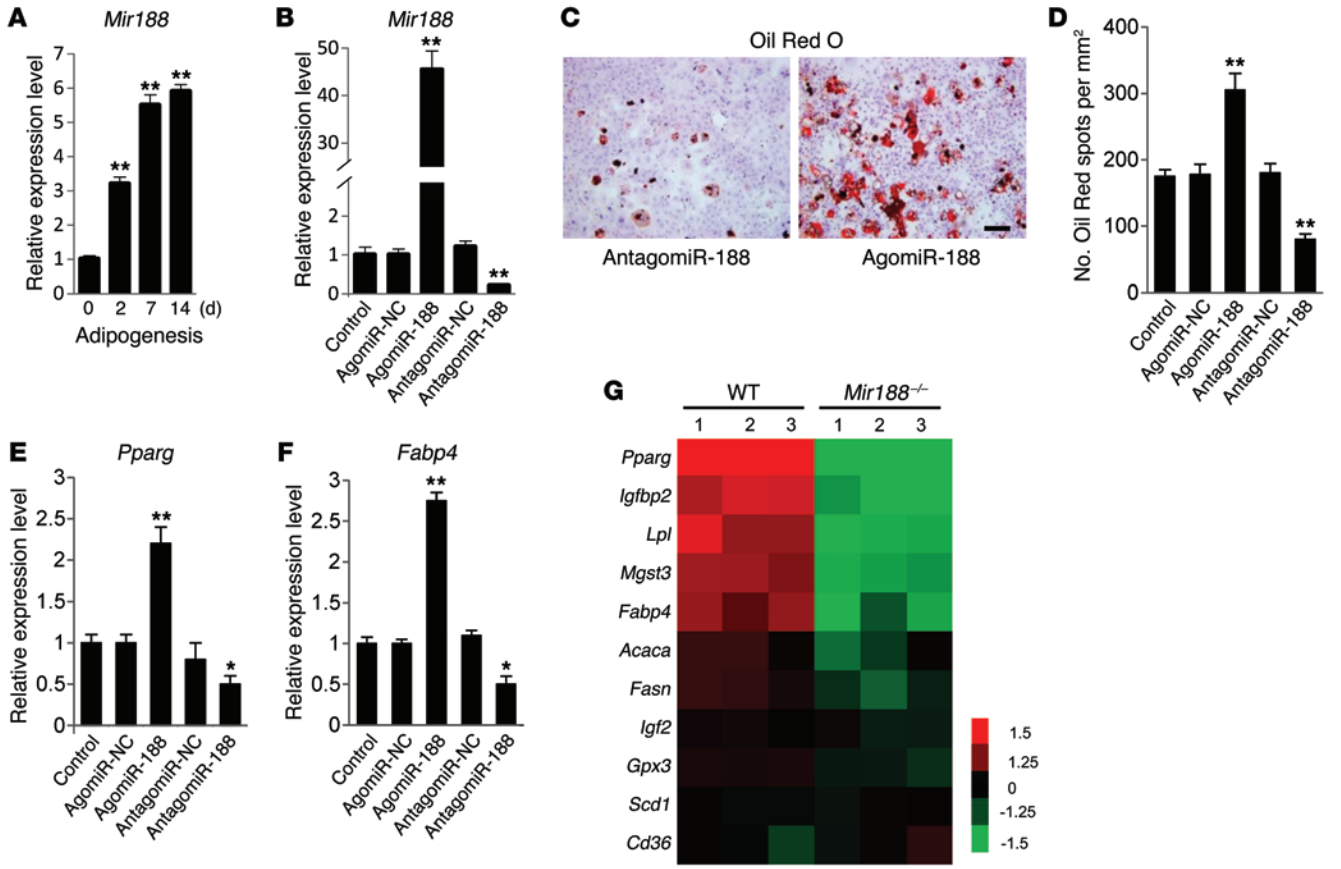

Figure 6. MiR-188 promotes adipogenic differentiation of BMSCs. (**A**) qRT-PCR analysis of the relative levels of miR-188 expression in BMSCs cultured in adipogenesis induction medium (0.5 mM 3-isobutyl-1-methylxanthine, 5 μg/ml insulin, and 1 μM dexamethasone) for the days as indicated. *n* = 5 per group. (**B**) qRT-PCR analysis of the relative levels of miR-188 expression in BMSCs transfected with 10 μM agomiR-188, antagomiR-188, or their negative controls. NC, negative control. *n* = 5 per group. (**C** and **D**) Representative images of Oil Red O staining of lipids (**C**) and quantification of the number of spots (**D**) in BMSCs cultured in adipogenesis induction medium for 14 days. Scale bar: 100 μm. (**E** and **F**) qRT-PCR analysis of the relative levels of *Pparg* (**E**) and *Fabp4* (**F**) mRNA expression in BMSCs cultured in adipogenesis induction medium for 48 hours. (**G**) Microarray profiling results of dysregulated adipogenic genes in WT and *Mir188*$^{-/-}$ mouse–derived BMSCs cultured in adipogenesis induction medium for 48 hours. Data shown as mean ± SD. *$P < 0.05$, **$P < 0.01$ (ANOVA).

and other osteoblast differentiation markers were higher in osteoblastic induction medium–induced BMSCs of *Mir188*$^{-/-}$ mice as compared with their WT littermates (Figure 7H). The raw data of the microarray have been uploaded to GEO with the series record GSE63725 (http://www.ncbi.nlm.nih.gov/geo/query/acc.cgi?acc=GSE63725). All of these results suggest that miR-188 inhibits osteogenic differentiation of BMSCs.

MiR-188 directly targets HDAC9 and Rictor. MiRNAs regulate the expression of mRNAs by binding to the 3′-untranslated regions (3′-UTRs) or amino acid coding sequences of target genes. We used miRanda (19), PicTar (20), and TargetScan (21) to predict the targets of miR-188. Among the predicted genes, we chose 6 for further analysis—histone deacetylase 9 (*Hdac9*), RPTOR-independent companion of MTOR complex 2 (*Rictor*), phosphatase and tensin homolog (*Pten*), zinc finger protein 281 (*Znf281*), GLIS family zinc finger 3 (*Glis3*), and ephrin B2 (*Efnb2*)—which had been reported to participate in bone metabolism (22–28). Overexpression or inhibition of miR-188 changed endogenous levels of HDAC9 and RICTOR protein, but not the others (Figure 8A). However, no changes of the mRNA levels of *Hdac9* and *Rictor* were noted (Supplemental Figure 7).

Sequence analysis revealed 1 conserved binding site for miR-188 in the 3′-UTR of the *HDAC9* gene (position 1914–1921) and 2 in the *RICTOR* gene (position 3761–3767, position 4112–4118) (Figure 8B). To investigate whether miR-188 directly targets HDAC9 and RICTOR, luciferase reporter constructs containing the predicted miRNA-binding site of HDAC9 and RICTOR (WT-pGL3-HDAC9, WT1-pGL3-RICTOR, or WT2-pGL3-RICTOR) were generated (Supplemental Table 1). We transfected WT-pGL3-HDAC9, WT1-pGL3-RICTOR, or WT2-pGL3-RICTOR with agomiR-188 or agomiR-NC into BMSCs and measured the effects of miR-188 on luciferase translation by the level of luciferase enzyme activity. Overexpression of miR-188 suppressed the luciferase activity of the *Hdac9* or *Rictor* 3′-UTR reporter genes (Figure 8, C–E). Mutation of 2 nucleotides within the sequences of the putative target site in the 3′-UTR of *Hdac9* or *Rictor* (MUT-pGL3-HDAC9, MUT1-pGL3-RICTOR, or MUT2-pGL3-RICTOR) abolished this repression, confirming the specificity of miR-188's action (Figure 8, C–E).

We also detected the protein of HDAC9 or RICTOR in BMSCs of aged (18 months) and young (3 months) WT and *Mir188*$^{-/-}$ mice. HDAC9 and RICTOR protein levels were lower in 18-month-old WT mice compared with 3-month-old WT mice, while in *Mir188*$^{-/-}$

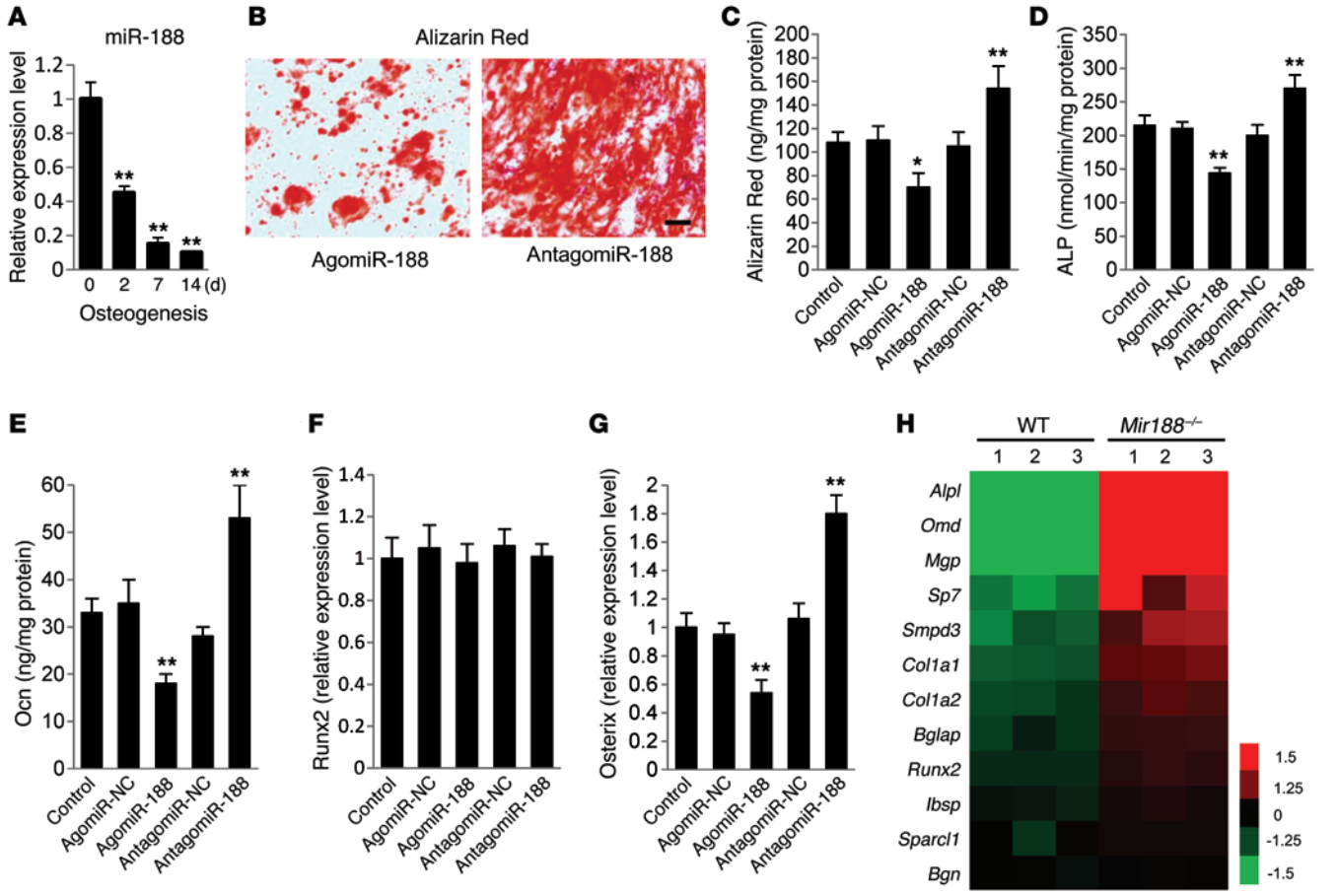

Figure 7. MiR-188 inhibits osteogenic differentiation of BMSCs. (**A**) qRT-PCR analysis of the relative levels of miR-188 expression in BMSCs cultured in osteogenesis induction medium (300 ng/ml BMP-2, 50 μg/ml ascorbic acid, and 5 mM β-glycerolphosphate) for the days as indicated. *n* = 5 per group. (**B** and **C**) Representative images of Alizarin Red S staining (**B**) and quantitative analysis (**C**) of matrix mineralization in BMSCs transfected with agomiR-188, antagomiR-188, or their controls and cultured in osteogenesis induction medium for 21 days. *n* = 5 per group. Scale bar: 100 μm. (**D** and **E**) Analysis of ALP activity (**D**) and osteocalcin secretion (**E**) in BMSCs cultured in osteogenesis induction medium for 48 hours. (**F** and **G**) qRT-PCR analysis of the relative levels of osterix (**F**) and *Runx2* (**G**) mRNA expression in BMSCs cultured in osteogenesis induction medium for 48 hours. *n* = 5 per group. (**H**) Microarray profiling results of dysregulated osteogenic genes in WT and *Mir188*$^{-/-}$ mouse–derived BMSCs cultured in osteogenesis induction medium for 48 hours. Data shown as mean ± SD. *$P < 0.05$, **$P < 0.01$ (ANOVA).

mice, HDAC9 and RICTOR protein levels were similar in young and aged mice (Figure 8F). However, HDAC9 and RICTOR protein levels were significantly lower in miR-188 transgenic mice compared with their WT littermates (Figure 8F).

Whether the miR-188 targets in *HDAC9* and *RICTOR* are preserved in humans was also investigated. Sequence analysis revealed that binding sites for hsa-miR-188 in the 3′-UTR of human *HDAC9* (position 1905–1912) and *RICTOR* (position 4344–4351) are conserved in mice (Supplemental Figure 8, A and B, and Supplemental Table 1). Luciferase reporter constructs containing the predicted miRNA-binding site of the human HDAC9 and RICTOR (WT-pGL3-hHDAC9 and WT-pGL3-hRictor) were generated (Supplemental Figure 8B) and then transfected into human BMSCs with agomiR-188 or agomiR-NC. Overexpression of miR-188 suppressed the luciferase activity of the human *HDAC9* or *RICTOR* 3′-UTR reporter gene (Supplemental Figure 8, C and D). Mutation of the 2 nucleotides within the sequences of the putative target site in the 3′-UTR of human *HDAC9* or *RICTOR* (MUT-pGL3-hHDAC9, MUT-pGL3-hRICTOR) abolished this repression, confirming the specificity of the action (Supplemental Figure 8, C and D). Furthermore, human BMSCs with transfection of agomiR-188 or antagomiR-188 showed that overexpression of miR-188 decreased endogenous HDAC9 or RICTOR protein while inhibition of miR-188 increased their protein levels (Supplemental Figure 8E).

These results demonstrate that HDAC9 and RICTOR are the targets of miR-188 in both mouse and human.

Injection of antagomiR-188 into bone marrow stimulates bone formation and decreases bone marrow fat in aged mice. To investigate the therapeutic effects of BMSC-specific inhibition of miR-188 on age-related osteoporosis, aptamer-antagomiR-188 was injected into the femoral bone marrow cavity of 15-month-old mice twice per month for 3 months. Intra–bone marrow injection of BMSC-targeting aptamer-antagomiR-188 significantly decreased the levels of miR-188 in BMSCs (Figure 9A). Aptamer-antagomiR-188 increased the trabecular bone volume, number, and cortical bone thickness, and decreased trabecular separation and the endosteal perimeter (Figure 9, B–I). Furthermore, bone strength increased in those mice that received aptamer-antagomiR-188 treatment (Fig-

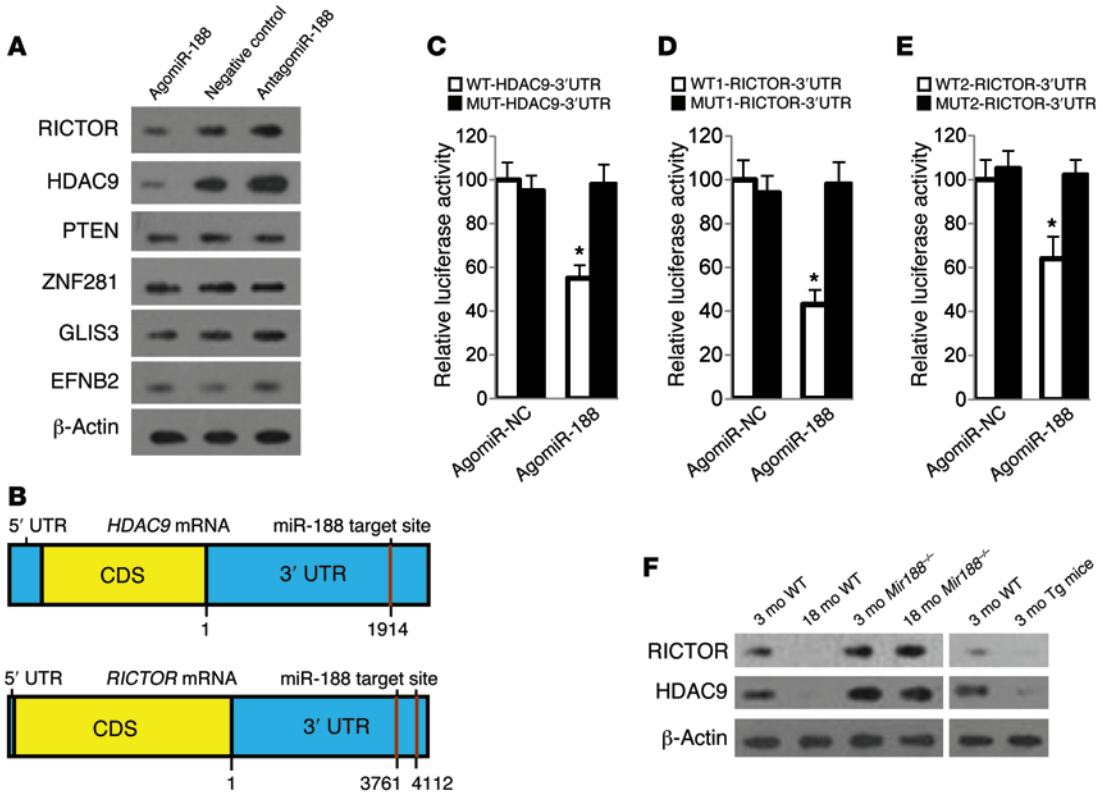

Figure 8. MiR-188 directly targets HDAC9 and RICTOR. (**A**) Western blot analysis of the relative levels of HDAC9, RICTOR, PTEN, ZNF281, GLIS3, and EFNB2 protein expression in BMSCs transfected with agomiR-188 and antagomiR-188. β-Actin was used as loading control. Data are representative of 3 independent experiments. (**B**) Schematic of miR-188 putative target sites in mouse *Hdac9* and *Rictor* 3′-UTR. CDS, coding sequence. (**C**–**E**) BMSCs were transfected with luciferase reporter carrying WT or MUT 3′-UTR of the *HDAC9* gene (WT–HDAC9–3′-UTR and MUT–HDAC9-3′–UTR) (**C**) WT1–Rictor–3′-UTR and MUT1–Rictor–3′-UTR (**D**), WT2–Rictor–3′-UTR and MUT2–Rictor–3′-UTR (**E**), respectively, and cotransfected with agomiR-188 or agomiR-NC. Effects of miR-188 on the reporter constructs were determined at 48 hours after transfection. Firefly luciferase values, normalized for renilla luciferase, are presented. $n = 3$ per group. (**F**) Western blot analysis of HDAC9 and RICTOR protein expression in BMSCs from different mice as indicated. Data are representative of 3 independent experiments. Data shown as mean ± SD. $^*P < 0.01$ vs. MUT-pGL3-HDAC9 or -RICTOR (Student's *t* test).

ure 9, J and K). Notably, trabecular and endosteal BFR increased in mice treated with aptamer-antagomiR-188 (Figure 9, L–N). Aptamer-antagomiR-188 also decreased the number and area of adipocytes in bone marrow, and increased the number and surface of osteoblasts on trabecular and endosteal bone surfaces (Figure 9, O–R, and Supplemental Figure 9, A and B). However, there were no differences of number and surface of osteoclasts on the trabecular bone surface (Supplemental Figure 9B).

These results suggest that intra–bone marrow injection of antagomiR-188 would prevent bone loss and marrow fat accumulation in aged mice.

Discussion

BMSCs tend to differentiate into adipocytes rather than osteoblasts with aging, which leads to progressive accumulation of fat and bone loss (3–7). Here we demonstrated that miR-188 is involved in this shift of cell lineage commitment of BMSCs, using *Mir188* knockout and overexpression transgenic mice. Furthermore, inhibiting miR-188 with a BMSC-specific delivery system reduced fat accumulation and promoted trabecular and cortical-endosteal bone formation in aged mice.

Several miRNAs have been reported to regulate BMSC lineage commitment (8–12). However, the roles of miRNAs in the age-related switch between osteoblast and adipocyte differentiation in bone marrow remain unclear. In this study, we revealed elevated miR-188 expression in BMSCs from aged mice and human subjects. Furthermore, *Mir188*$^{-/-}$ mice showed reduced age-associated bone loss and marrow fat accumulation. Osterix$^+$ osteoprogenitor-specific miR-188 transgenic mice showed accelerated bone marrow fat accumulation and bone loss. These results reveal that miR-188 regulates the differentiation directions of BMSCs during aging and contributes to age-related bone loss.

Previously, it was reported that miR-188 regulates dendritic plasticity and synaptic transmission (29), and suppresses G1/S transition (30). However, there is no report on the role of miR-188 in the regulation of BMSC function. In this study, we defined a new mechanism whereby miR-188 regulates the BMSC switch in bone. MiRNAs mediate post-transcriptional gene silencing by base pairing to the complementary sites in the 3′-UTR of the target mRNA (31). We demonstrated that miR-188 directly targets *Hdac9* and *Rictor* mRNAs. HDAC9, which is dramatically downregulated during adipogenesis, inactivates PPARγ to repress adipogenesis and promote osteogenesis of BMSCs (22, 23). RICTOR, as a key component of mTORC2, which is a member of the mTOR complex implicated in resting cytoskeletal architecture, suppresses PPARγ activity and inhibits adipogenic differentia-

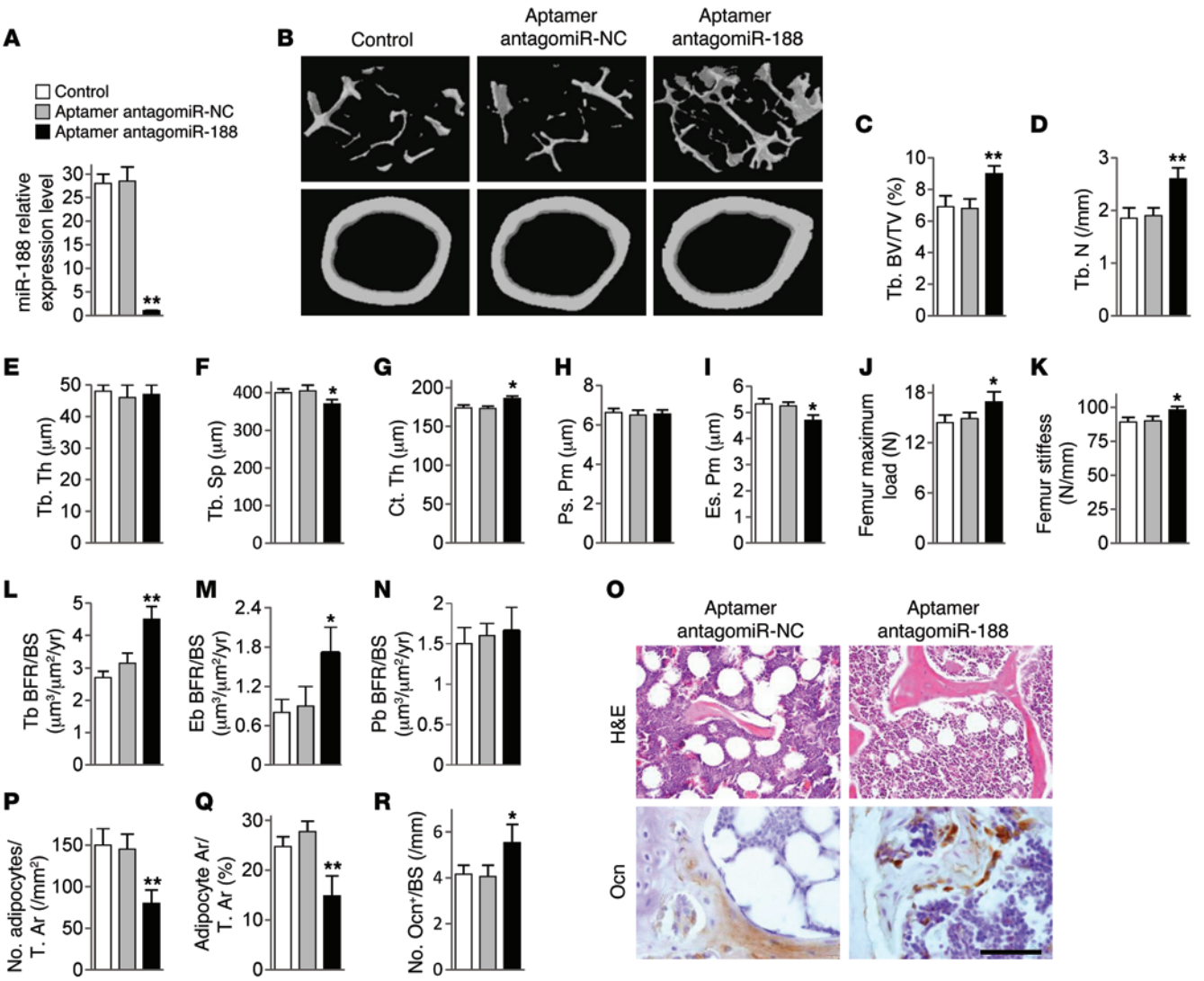

Figure 9. Injection of aptamer-antagomiR-188 into bone marrow stimulates bone formation and decreases marrow fat accumulation in aged mice. (**A**) qRT-PCR analysis of the levels of miR-188 expression in BMSCs of mice with BMSC-specific antagomiR-188 delivery. Aptamer-antagomiR-188 was injected into femoral bone marrow cavity of 15-month-old mice twice per month for 3 months. NC, negative control. (**B**–**I**) Representative μCT images (**B**) and quantitative μCT analysis of trabecular (**C**–**F**) and cortical (**G**–**I**) bone microarchitecture in femora from aptamer-treated mice. *n* = 10 per group. (**J** and **K**) Three-point bending measurement of femur maximum load (**J**) and stiffness (**K**). *n* = 5 per group. (**L**–**N**) Calcein double labeling–based quantification of bone formation rate per bone surface (BFR/BS) in femora. *n* = 5 per group. (**O**–**R**) Representative images of H&E staining (**O**, top) and osteocalcin immunohistochemical staining (**O**, bottom) and quantification of number and area of adipocytes (**P** and **Q**) and number of osteoblasts (**R**) in distal femora. Scale bars: 100 μm. *n* = 5 per group. Data shown as mean ± SD. $^*P < 0.05$, $^{**}P < 0.01$ (ANOVA).

tion of mesenchymal stem cells (24). The present study showed that miR-188 post-transcriptionally inhibits HDAC9 and Rictor expression and upregulates PPARγ expression during adipogenic differentiation of BMSCs.

Thus, the observation that translations of *Hdac9* and *Rictor* are inhibited by miR-188 provides a molecular link to the age-related switch between osteoblast and adipocyte differentiation. During aging, miR-188 expression is induced in BMSCs. MiR-188 suppresses the production of HDAC9 and Rictor in BMSCs, which activates the adipogenic transcription factor PPARγ. Consequently, BMSCs favor differentiation into adipocytes, resulting in an increased number of adipocytes and a decreased number of osteoblasts, causing age-related bone loss. Thus, our study revealed a new mechanism whereby miR-188 regulates the differentiation of BMSCs during aging.

With the progressive aging of the general population, age-related bone loss becomes a growing public problem (32). A major requirement for the treatment of age-related bone loss is to identify anabolic agents that can increase bone formation and decrease fat accumulation in bone marrow via targeting BMSCs (33). In this study, we identified a new mechanism for developing this treatment. We used a BMSC-specific aptamer to deliver antagomiR-188 or agomiR-188 into mice BMSCs. Aptamers are single-stranded nucleic acid molecules that bind to targets via folding into a 3-dimensional structure with high affinity and selectivity (34, 35). Cell type–specific aptamers as drug delivery vehicles have been exploited to enhance the efficacy and safety of therapeutic drugs used in cancer (36, 37), HIV (38, 39), and eye-related diseases (40). Treatment with antagomiR-188 via a BMSC-specific aptamer increased bone

formation and decreased bone marrow fat accumulation in aged mice, while treatment with agomiR-188 led to premature aging of bone in middle-aged mice, as evidenced by reduced bone formation and increased bone marrow fat. Currently, most drugs for osteoporosis that are available in the clinic inhibit bone resorption without increasing bone formation (41). Our results indicate that inhibition of miR-188 expression in BMSCs via an aptamer might be a new strategy to treat age-related bone loss and senile osteoporosis.

In conclusion, the current findings support the view that the age-related increase in miR-188 functions as a switch to regulate BMSC differentiation. The results reveal a new mechanism of age-related bone loss and identify a potential therapeutic target.

Methods

Construction of Mir188$^{-/-}$ mice using TALEN plasmids. The miR-188–specific TALEN plasmids were obtained from Beijing ComWin Biotech Co. Ltd. The target TALEN sequences of the *Mir188* were: left, 5′-CCCTGCTCCCTCTCTCAC-3′, and right, 5′-CAGAGAGCTCACCCTC-3′. TALEN plasmids were digested by NotI restriction endonuclease. The digested plasmids were transcribed to mRNA in vitro using the mMESSAGE mMACHINE T7 Kit (Life Technologies), according to the manufacturer's instructions. We purified the synthesized mRNAs using a MegaClear Kit (Life Technologies), according to the manufacturer's instruction. The mRNAs were diluted to working concentration (50 ng/μl) in injection buffer (0.25 mM EDTA, 10 mM Tris, pH 7.4) treated with diethyl pyrocarbonate (Sigma-Aldrich).

C57BL/6 mice were used as embryo donors and were superovulated. The TALEN mRNAs were injected into the cytoplasm of pronuclear-stage fertilized eggs, which were obtained from oviducts after superovulated female C57BL/6 mice were mated to C57BL/6 stud males. The injected zygotes were cultured in M2 medium (Sigma-Aldrich) at 37°C for 24 hours. Zygotes that developed into the 2-cell stage were selected to transfer into the oviducts of pseudopregnant imprinting control region (ICR) female mice.

Genomic DNA was extracted from tail tips. For genotyping of miR-188, PCR was carried out using the following primers (synthesized by Sangon Biotech): forward, 5′-TCTTGGTCCGCATGTGTGTG-3′, and reverse, 5′-AGGGAGTTCAAAGGCAGCATG-3′. To determine the accuracy of PCR, we collected the PCR products from agarose gel to use as templates for sequencing.

Generation of osterix^{+} osteoprogenitor-specific miR-188 transgenic mice. To generate osterix^{+} osteoprogenitor-specific miR-188 transgenic (miR-188-Tg) mice, a plasmid containing the osterix promoter to drive gene expression was constructed. First, we subcloned the mouse pre-mir-188 cDNA (synthesized by Genscript Co.) into the SalI-EcoRI site in a plasmid containing the osterix promoter, resulting in osterix-pre-mir-188 vector. The plasmid (osterix-pre-miR-188) was then transfected into BMSCs using Lipofectamine 2000 (Invitrogen). Empty vector was also transfected into BMSCs as a control. qRT-PCR was used to detect the expression of miR-188. The fragments of the osterix-pre-mir-188 were then purified and microinjected into C57BL/6J F_2 mouse oocytes, and the oocytes were then surgically transferred into pseudopregnant C57BL/6J dams. Two lines with high levels of miR-188 expression were selected from 5 transgenic founders and bred in C57BL/6 strain for 6 generations to obtain offspring with a defined genetic background. One line with a sevenfold overexpression of miR-188 was extensively studied. The WT mice were used as controls.

All mice were maintained in the specific pathogen–free facility of the Laboratory Animal Research Center at Central South University.

BMSC isolation and culture. For mouse BMSC isolation, bone marrow cells were flushed from femora of female mice and incubated for 20 minutes at 4°C with PE-, FITC-, peridinin chlorophyll protein–, and allophycocyanin-conjugated antibodies that recognized mouse Sca-1 (108108; BioLegend), CD29 (102206; BioLegend), CD45 (103132; BioLegend), and CD11b (101226; BioLegend). For human BMSC isolation, human bone marrow cells were incubated with FITC-, allophycocyanin-, and PE-conjugated antibodies that recognized human STRO-1 (catalog 340106; BioLegend), CD45 (catalog 304012; BioLegend), and CD146 (catalog 361008; BioLegend) at 4°C for 30 minutes. Acquisition was performed on a FACS Aria model (BD Biosciences), and the analysis was performed using FACS DIVE software version 6.1.3 (BD Biosciences).

The sorted mouse CD29^{+}Sca-1^{+}CD45^{-}CD11b^{-} BMSCs and human CD146^{+}STRO-1^{+}CD45^{-} BMSCs were cultured for 1–2 weeks to reach 80%–85% confluence. Then, first-passage BMSCs were detached and seeded in culture flasks for enrichment of cell populations. As second-passage BMSCs reached confluence after approximately 1 week, they were subcultured. Only third-passage BMSCs were subjected to induction of adipogenic and osteogenic differentiation, and transfection of plasmids.

MiRNA microarray assay. Small RNAs were isolated from the total RNA of BMSCs from young (3 months old) and aged (18 months old) female C57BL/6 mice, and then labeled with Cy3. The Oebiotech Company performed the miRNA microarray assay. The fragmentation mixtures were hybridized to an Agilent-046065 Mouse miRNA Microarray V19.0 8×60K (Agilent). Feature Extraction software 10.7.1.1 (Agilent) analyzed the scanned images using default parameters to obtain background subtracted and spatially detrended processed signal intensities as the raw data. Raw data were normalized in a quantile algorithm with Genespring 12.0 (Agilent). Probes for which at least 100% of samples in any 1 condition out of 2 conditions had flags in "Detected" were maintained. The raw data of the microarray have been uploaded to GEO with the series record GSE57127.

Gene chip microarray assay. RNAs were isolated from WT and *Mir188$^{-/-}$* mouse–derived BMSCs cultured with adipogenesis induction medium or osteogenesis induction medium for 48 hours. The RNAs were sent to the UCLA Clinical Microarray Core to perform the gene chip microarray assay. The fragmentation mixtures were hybridized to an Affymetrix mouse 1.0 gene ST array. Robust multiarray average was used to perform the data normalization. Principal component analysis in Partek Genomics Suite was used to perform the cluster analysis of different samples. ANOVA was used to identify the differential expression genes. The raw data of the microarray have been uploaded to GEO with the SuperSeries record GSE63725.

Histochemistry analysis. Histochemistry analysis was performed as described previously (42, 43). Briefly, femora were harvested from mice after euthanasia, fixed in 10% formalin for 24 hours, and decalcified in 10% EDTA for 14 days, before being embedded in paraffin. Four-micrometer-thick longitudinally oriented bone sections were stained with H&E, TRAP, and toluidine blue to quantify number and surface of osteoblasts, number and surface of osteoclasts, and number and area of adipocytes, respectively.

OsteoMeasureXP Software (OsteoMetrics Inc.) performed histomorphometric measurements of 2-dimensional parameters of the

trabecular bones. To label the mineralization fronts, the mice were injected with 25 mg/kg calcein at 8 and 2 days before euthanasia. The femora were fixed in 70% ethanol and dehydrated in increasing concentrations of ethanol, and the undecalcified bones were embedded in methyl methacrylate. Serial 5-μm sections of the femur were made using a microtome. The parameters obtained for the bone formation were bone formation rate per bone surface, osteoblast surface per bone surface, and osteoblast number per bone perimeter. The parameters measured for bone resorption were osteoclast surface per bone surface and osteoclast number per bone perimeter.

Immunohistochemical staining. Immunohistochemical staining was performed as described previously (44, 45). Briefly, bone sections were processed for antigen retrieval by digestion with 0.05% trypsin at 37°C for 15 minutes, and then incubated with primary antibody against osteocalcin (catalog M173; Takara) overnight at 4°C. Subsequently, an HRP-streptavidin detection system (Dako) was used to detect the immunoactivity, followed by counterstaining with hematoxylin (Sigma-Aldrich). Sections incubated with polyclonal rabbit IgG (R&D Systems Inc.) served as negative controls.

Identification of an aptamer using cell-SELEX procedure. The selection technology to generate aptamers is called systematic evolution of ligands by exponential enrichment (SELEX) (16–18). The library of synthetic DNAs comprised a 40-base central random sequence flanked by primer sites on either side (5′-GAATTCAGTCGGACAGCG-N40-GATGGACGAATATCGTCTCCC-3′). Four-nanomole single-stranded DNA (ssDNA) pools were denatured by heating to 80°C for 10 minutes in a selection buffer containing 50 mM Tris-HCl (pH 7.4), 5 mM KCl, 100 mM NaCl, 1 mM $MgCl_2$, and 0.1% NaN_3 and then renatured at 0°C for 10 minutes. The mouse BMSCs, monocytes/macrophages, or preosteoclasts (10^6 cells for the first round and 10^5 cells for the further rounds) were incubated with the ssDNA at 37°C for 30 minutes in selection buffer. Partitioning of bound and unbound ssDNA sequences was done by centrifugation. After centrifugation and washing 3 times with 1 ml selection buffer (with 0.2% BSA), cell-bound ssDNAs were amplified by PCR. Aptamers obtained from the tenth round of selection were PCR-amplified using unmodified primers and cloned into *E. coli* using the TA Cloning Kit (Promega Corp.). The plasmids of individual clones were isolated with a Plasmid Extraction Kit (QIAGEN), and the inserts were PCR-amplified and sequenced. The sequence of the aptamer that showed the highest binding affinity to mouse BMSCs was 5′-GAATTCAGTCGGACAGCGACGACGGTGATATGTCAAGGTCGTATGCACGAGTCAGAGGGATGGACGAATATCGTCTCCC-3′.

For flow cytometry analysis, cultured BMSCs, monocytes/macrophages, and preosteoclasts were washed with PBS and detached with nonenzymatic dissociation buffer for 15 minutes. After washing, the cells were incubated with a FITC-labeled ssDNA pool dissolved in 200 μl binding buffer at a final concentration of 250 nM for 45 minutes. Cells were washed twice with 1 ml washing buffer and resuspended in 200 μl binding buffer. Fluorescence was determined with a FACScan cytometer (BD Immunocytometry Systems).

Construction of BMSC-specific aptamer delivery system. The BMSC-specific aptamer was synthesized by Genscript Co. AgomiR-188, antagomiR-188, and their respective negative controls (NCs) were synthesized by RiboBio Co.

We mixed 1 part by volume of a polyethyleneimine (PEI) solution (100 μg/ml, pH 6.0) with 6 parts by volume of a 4.2-μM sodium citrate to form the PEI-citrate core structure (nanocore). Then, we added 3 parts by volume of synthetic BMSC aptamers (50 nM) and agomiR-188 (1 μM) or antagomiR-188 (1 μM) to the nanocore for 5 minutes of reaction to assemble the nanocomplex.

Mice received either 40 μl of an agomiR-188 nanocomplex or an antagomiR-188 nanocomplex, or a comparable volume of PBS via periosteal injection into medullary cavity of femur twice per month for 3 months.

mRNA 3′-UTR cloning and luciferase reporter assay. For functional analysis of miR-188, the segments of the mouse and human *HDAC9* and *Rictor* 3′-UTR, including the predicted miR-188–binding site, were PCR-amplified. The PCR products were purified and inserted into the XbaI-FseI site immediately downstream of the stop codon in the pGL3 control luciferase reporter vector (Promega Corp.), resulting in mouse and human WT-pGL3-HDAC9, WT1-pGL3-RICTOR, or WT2-pGL3-RICTOR. The HDAC9 and RICTOR mutants for the miR-188 seed regions were prepared using the QuikChange Site-Directed Mutagenesis Kit (Stratagene) to get mouse and human MUT-pGL3-HDAC9, MUT1-pGL3-RICTOR, or MUT2-pGL3-RICTOR. Mouse and human BMSCs were transfected with either WT or mutant pGL3 construct, the pRL-TK renilla luciferase plasmid (Promega Corp.), and agomiR-188 or agomiR-NC for 48 hours using Lipofectamine 2000 (Invitrogen). The dual luciferase reporter assay system (Promega Corp.) was used to quantify luminescent signal using a luminometer (Glomax; Promega Corp.). Each value from the firefly luciferase assay was normalized to the renilla luciferase value from the cotransfected phRL-null vector (Promega Corp.). The nucleotide sequences of primers for WT and mutant reporter plasmids are shown in Supplemental Table 2.

Adipogenic differentiation assay. To induce adipogenic differentiation of BMSCs in vitro, BMSCs were cultured in 6-well plates at 2.5×10^6 cells per well with adipogenesis induction medium (α-MEM containing 10% FCS, 0.5 mM 3-isobutyl-1-methylxanthine, 5 μg/ml insulin, and 1 μM dexamethasone) for 14 days. Culture medium was changed every second day. We performed Oil Red O staining to detect mature adipocytes in cultures with adipogenesis induction.

Osteogenic differentiation and mineralization assay. To induce osteoblastic differentiation, BMSCs were cultured in 24-well plates at 5×10^5 cells per well with osteogenesis induction medium (300 ng/ml BMP-2, 50 μg/ml ascorbic acid, and 5 mM β-glycerolphosphate) for 48 hours. Then, the cell lysates were homogenized for ALP activity assay by spectrophotometric measurement of *p*-nitrophenol release using an enzymatic colorimetric ALP Kit (Roche). Culture media were collected for assessment of secreted osteocalcin levels using a specific immunoassay kit (DiaSorin).

To induce osteoblastic mineralization, BMSCs were cultured in 6-well plates at 2.5×10^6 cells per well with osteogenesis induction medium, as described above, for 21 days. Then, cells were stained with 2% Alizarin Red S (Sigma-Aldrich) at pH 4.2 to evaluate the cell matrix mineralization. A Diaphot Inverted Microscope and Camera System (Nikon) was used for imaging. Alizarin Red S released from the cell matrix into the cetyl-pyridinium chloride solution was quantified by spectrophotometry at 540 nm.

To normalize protein expression to total cellular protein, a fraction of the lysate solution was subjected to the Bradford assay.

Preosteoclast and osteoclast differentiation. Monocytes and macrophages were harvested from bone marrow of 6-month-old female WT and *Mir188*$^{-/-}$ mice by flushing of the femur and tibia marrow space.

Flushed bone marrow cells were cultured on Petri dishes in α-MEM containing 10% FBS, 100 U/ml penicillin, 100 μg/ml streptomycin sulfate, and 30 ng/ml M-CSF (R&D Systems Inc.) overnight. After discarding of the adherent cells, floating cells were incubated with M-CSF (30 ng/ml) to obtain monocytes and macrophages. Monocytes and macrophages were further cultured in 24-well plates (1×10^5 cells per well) with 30 ng/ml M-CSF and 60 ng/ml RANKL (PeproTech) for 3 days to obtain preosteoclasts. Alternatively, we incubated monocytes and macrophages with 30 ng/ml M-CSF and 200 ng/ml RANKL for 8 days to obtain fully mature multinucleated osteoclasts. TRAP activities of the preosteoclasts and osteoclasts were detected using a commercial kit (Sigma-Aldrich).

qRT-PCR analysis. We performed qRT-PCR using a Roche Molecular Light Cycler as previously described (46, 47). Total RNA from tissues or cultured cells was isolated using the TRIzol reagent (Invitrogen), and reverse transcription was performed using 1 μg total RNA and SuperScript II (Invitrogen). Amplification reactions were set up in 25-μl reaction volumes containing SYBR Green PCR Master Mix (PE Applied Biosystems) and amplification primers. A 1-μl volume of cDNA was used in each amplification reaction. Primer sequences are listed in Supplemental Table 3 and Supplemental Table 4.

Western blot. We performed Western blotting as previously described (46). Total cell lysates were separated by SDS-PAGE blotted on PVDF membranes (Millipore). The membranes were incubated with specific antibodies to HDAC9 (ab18970; Abcam), RICTOR (ab70374; Abcam), PTEN (ab32199; Abcam), ZNF281 (ab112047; Abcam), GLIS3 (NBP1-80417; Novus Biologicals), EFNB2 (ab131536; Abcam), or β-actin (ab3280; Abcam), then reprobed with appropriate HRP-conjugated secondary antibodies. Blots were developed using an ECL Kit (Santa Cruz), and exposed to x-ray films.

Microcomputed tomography analysis. The right femora and lumbar spines dissected from mice were fixed with 4% PFA for 24 hours, then scanned and analyzed with a GE Explore Locus SP microcomputed tomography (μCT) system (GE Healthcare Co.). X-ray voltage and current were set to 80 kV and 80 μA, respectively, with a resolution of 12 μm per pixel. Cross-sectional images of distal femur and L4 vertebra were used to perform 3-dimensional histomorphometric analysis of trabecular bone. For the distal femur, the region of interest (ROI) selected for analysis was 5% of femoral length from 0.1 mm below the growth plate to determine trabecular bone volume per tissue volume (Tb. BV/TV), trabecular number (Tb. N), trabecular separation (Tb. Sp), and trabecular thickness (Tb. Th). For L4 vertebra, the entire region of the trabecular bone was selected for analysis to determine the trabecular bone volume per tissue volume (Vt. BV/TV). Cross-sectional images of the mid-diaphysis of femur were used to perform 3-dimensional histomorphometric analysis of cortical bone. For cortical bone, the ROI selected for analysis was of 10% of femoral length in mid-diaphysis of the femur to determine cortical thickness (Ct. Th), periosteal perimeter (Ps. Pm), and endosteal perimeter (Es. Pm).

Three-point bending test. The cortical strength of the tibia and femur at the midshaft location was measured using a 3-point bending test on a mechanical-testing machine (WDW3100; Changchun, China) equipped with a 500 N M-SI sensor (Celtron Technologies Inc.). For the 3-point bending test, there are 2 end support points and 1 central loading point. The span length between 2 support points was 60% of the total bone length. Each bone was loaded at a constant speed of 0.155 mm/s until failure. The biomechanical measurement data were collected from the load-deformation curves. The maximum load (N) and stiffness (N/mm) were recorded.

Study population. Human bone marrow samples were obtained from 48 patients (20 male and 28 female) with osteoarthritis undergoing knee joint replacement, with ages ranging from 54 to 82 years; 41 patients (27 male and 14 female) with femoral neck fracture and/or femoral head fractures undergoing hip joint replacement, with ages ranging from 50 to 89 years; and 54 patients (25 male and 29 female) with tibia fractures and 27 patients (13 male and 14 female) with femur shaft fracture undergoing open reduction internal fixation, ranging in age from 20 to 70 years (human bone marrow aspiration and collection were conducted by the Orthopedic Surgery Department at the Second Xiangya Hospital of Central South University). One hundred seventy patients (85 male and 85 female) were selected on the basis of the inclusion and exclusion criteria. All subjects were screened using a detailed questionnaire, disease history, and physical examination. Subjects were excluded from the study if they had had conditions affecting bone metabolism, including diseases of the kidney, liver, parathyroid, or thyroid, diabetes mellitus, hyperprolactinemia, oophorectomy, rheumatoid arthritis, ankylosing spondylitis, malabsorption syndromes, malignant tumors, hematological diseases, or previous pathological fractures, within the past year. If the subjects had received treatment with glucocorticoids, estrogens, thyroid hormone, parathyroid hormone, fluoride, bisphosphonate, calcitonin, thiazide diuretics, barbiturates, or antiseizure medication, they were also excluded. These participants underwent bone marrow aspiration and collection during bone fracture surgery and joint replacement.

Statistics. Data are presented as mean ± SD. For comparisons of 2 groups, 2-tailed Student's *t* test was used. Comparisons of multiple groups were made using 1-way ANOVA. All experiments were repeated at least 3 times, and representative experiments are shown. Differences were considered significant at $P < 0.05$.

Study approval. All animal care protocols and experiments were reviewed and approved by the Animal Care and Use Committee of the Laboratory Animal Research Center at Xiangya Medical School of Central South University. All mice were maintained in the specific pathogen–free facility of the Laboratory Animal Research Center at Central South University. The clinical study was approved by the Ethics Committee of the Second Xiangya Hospital of Central South University, and written informed consent was obtained from all participants prior to bone marrow aspiration and collection.

Acknowledgments

The authors gratefully thank the Orthopedic Surgery Department at the Second Xiangya Hospital of Central South University for human bone marrow aspiration and collection. We acknowledge ELIXIGEN Co. for helping in editing and proofreading the English of the final manuscript. This work was supported by China National Funds for Distinguished Young Scientists grant 81125006. The raw data of the microarray have been uploaded in GEO, with the series records GSE57127 and GSE63725.

Address correspondence to: Xiang-Hang Luo, Er-Yuan Liao, or Hui Xie, Institute of Endocrinology and Metabolism, The Second Xiangya Hospital of Central South University, 139 Middle Renmin Road, Changsha, Hunan 410011, China. Phone: 86.731.85292152; E-mail: xianghangluo@hotmail.com (X.-H. Luo), eyliao_csu@sohu.com (E.-Y. Liao), or hxie5_csu@163.com (H. Xie).

1. Pittenger MF, et al. Multilineage potential of adult human mesenchymal stem cells. *Science*. 1999;284(5411):143–147.
2. Sekiya I, Larson BL, Vuoristo JT, Cui JG, Prockop DJ. Adipogenic differentiation of human adult stem cells from bone marrow stroma (MSCs). *J Bone Miner Res*. 2004;19(2):256–264.
3. Moerman EJ, Teng K, Lipschitz DA, Lecka-Czernik B. Aging activates adipogenic and suppresses osteogenic programs in mesenchymal marrow stroma/stem cells: the role of PPAR-γ2 transcription factor and TGF-β/BMP signaling pathways. *Aging Cell*. 2004;3(6):379–389.
4. Shen W, et al. MRI-measured pelvic bone marrow adipose tissue is inversely related to DXA-measured bone mineral in younger and older adults. *Eur J Clin Nutr*. 2012;66(9):983–988.
5. Yeung DK, Griffith JF, Antonio GE, Lee FK, Woo J, Leung PC. Osteoporosis is associated with increased marrow fat content and decreased marrow fat unsaturation: a proton MR spectroscopy study. *J Magn Reson Imaging*. 2005;22(2):279–285.
6. Kim VN, Han J, Siomi MC. Biogenesis of small RNAs in animals. *Nat Rev Mol Cell*. 2009;10(2):126–139.
7. Bartel DP. MicroRNAs: genomics, biogenesis, mechanism, and function. *Cell*. 2004;116(2):281–297.
8. Huang J, Zhao L, Xing L, Chen D. MicroRNA-204 regulates Runx2 protein expression and mesenchymal progenitor cell differentiation. *Stem Cells*. 2010; 28(2):357–364.
9. Zhang JF, et al. MiR-637 maintains the balance between adipocytes and osteoblasts by directly targeting Osterix. *Mol Biol Cell*. 2011;22(21):3955–3961.
10. Li H, et al. miR-17-5p and miR-106a are involved in the balance between osteogenic and adipogenic differentiation of adipose-derived mesenchymal stem cells. *Stem Cell Res*. 2013;10(3):313–324.
11. Huang S, et al. Upregulation of miR-22 promotes osteogenic differentiation and inhibits adipogenic differentiation of human adipose tissue-derived mesenchymal stem cells by repressing HDAC6 protein expression. *Stem Cells Dev*. 2012;21(13):2531–2540.
12. Liao L, et al. Redundant miR-3077-5p and miR-705 mediate the shift of mesenchymal stem cell lineage commitment to adipocyte in osteoporosis bone marrow. *Cell Death Dis*. 2013;4:e600.
13. Tang Y, et al. TGF-β1–induced migration of bone mesenchymal stem cells couples bone resorption with formation. *Nat Med*. 2009;15(7):757–765.
14. Marrelli M, Paduano F, Tatullo M. Cells isolated from human periapical cysts express mesenchymal stem cell-like properties. *Int J Biol Sci*. 2013;9(10):1070–1078.
15. Sung YH, et al. Knockout mice created by TALEN-mediated gene targeting. *Nat Biotechnol*. 2013;31(1):23–24.
16. Ray P, Rialon-Guevara KL, Veras E, Sullenger BA, White RR. Comparing human pancreatic cell secretomes by in vitro aptamer selection identifies cyclophilin B as a candidate pancreatic cancer biomarker. *J Clin Invest*. 2012;122(5):1734–1741.
17. Phillips CM, Meng X, Zhang L, Chretien JH, Urnov FD, Dernburg AF. Identification of chromosome sequence motifs that mediate meiotic pairing and synapsis in C. elegans. *Nat Cell Biol*. 2009;11(8):934–942.
18. Schäfer R, et al. Aptamer-based isolation and subsequent imaging of mesenchymal stem cells in ischemic myocard by magnetic resonance imaging. *Rofo*. 2007;179(10):1009–1015.
19. Betel D, Koppal A, Agius P, Sander C, Leslie C. Comprehensive modeling of microRNA targets predicts functional non-conserved and non-canonical sites. *Genome Biol*. 2010;11(8):R90.
20. Chen K, Rajewsky N. Natural selection on human microRNA binding sites inferred from SNP data. *Nat Genet*. 2006;38(12):1452–1456.
21. Garcia DM, Baek D, Shin C, Bell GW, Grimson A, Bartel DP. Weak seed-pairing stability and high target-site abundance decrease the proficiency of lsy-6 and other microRNAs. *Nat Struct Mol Biol*. 2011;18(10):1139–1146.
22. Chatterjee TK, et al. Histone deacetylase 9 is a negative regulator of adipogenic differentiation. *J Biol Chem*. 2011;286(31):27836–27847.
23. Chen YH, et al. yocyte enhancer factor-2 interacting transcriptional repressor (MITR) is a switch that promotes osteogenesis and inhibits adipogenesis of mesenchymal stem cells by inactivating peroxisome proliferator-activated receptor gamma-2. *J Biol Chem*. 2011;286(12):10671–10680.
24. Sen B, et al. mTORC2 regulates mechanically induced cytoskeletal reorganization and lineage selection in marrow-derived mesenchymal stem cells. *J Bone Miner Res*. 2014;29(1):78–89.
25. Guntur AR, Reinhold MI, Cuellar J Jr, Naski MC. Conditional ablation of Pten in osteoprogenitors stimulates FGF signaling. *Development*. 2011;138(7):1433–1444.
26. Seo KW, Roh KH, Bhandari DR, Park SB, Lee SK, Kang KS. ZNF281 knockdown induced osteogenic differentiation of human multipotent stem cells in vivo and in vitro. *Cell Transplant*. 2013;22(1):29–40.
27. Beak JY, Kang HS, Kim YS, Jetten AM. Krüppel-like zinc finger protein Glis3 promotes osteoblast differentiation by regulating FGF18 expression. *J Bone Miner Res*. 2007;22(8):1234–1244.
28. Zhao C, et al. Bidirectional ephrinB2-EphB4 signaling controls bone homeostasis. *Cell Metab*. 2006;4(2):111–121.
29. Lee K, et al. An activity-regulated microRNA, miR-188, controls dendritic plasticity and synaptic transmission by downregulating neuropilin-2. *J Neurosci*. 2012;32(16):5678–5687.
30. Wu J, et al. MicroRNA-188 suppresses G 1 /S transition by targeting multiple cyclin/CDK complexes. *Cell Commun Signal*. 2014;12(1):66.
31. Carthew RW, Sontheimer EJ. Origins and Mechanisms of miRNAs and siRNAs. *Cell*. 2009;136(4):642–655.
32. Curtis JR, Safford MM. Management of osteoporosis among the elderly with other chronic medical conditions. *Drugs Aging*. 2012;29(7):549–564.
33. Bermeo S, Gunaratnam K, Duque G. Fat and bone interactions. *Curr Osteoporos Rep*. 2014;12(2):235–242.
34. Tahiri-Alaoui A, Frigotto L, Manville N, Ibrahim J, Romby P, James W. High affinity nucleic acid aptamers for streptavidin incorporated into bi-specific capture ligands. *Nucleic Acids Res*. 2002;30(10):e45.
35. Šmuc T, Ahn IY, Ulrich H. Nucleic acid aptamers as high affinity ligands in biotechnology and biosensorics. *J Pharm Biomed Anal*. 2013;81–82:210–217.
36. Iida J, et al. DNA aptamers against exon v10 of CD44 inhibit breast cancer cell migration. *PLoS One*. 2014;9(2):e88712.
37. Thiel KW, et al. Delivery of chemo-sensitizing siRNAs to HER2+-breast cancer cells using RNA aptamers. *Nucleic Acids Res*. 2012;40(13):6319–6337.
38. D'Atri V, et al. New anti-HIV aptamers based on tetra-end-linked DNA G-quadruplexes: effect of the base sequence on anti-HIV activity. *Chem Commun (Camb)*. 2012;48(76):9516–9518.
39. Zhou J, Li H, Zhang J, Piotr S, Rossi J. Development of cell-type specific anti-HIV gp120 aptamers for siRNA delivery. *J Vis Exp*. 2011;52(52):2954.
40. Subramanian N, et al. Target-specific delivery of doxorubicin to retinoblastoma using epithelial cell adhesion molecule aptamer. *Mol Vis*. 2012;18:2783–2795.
41. Martin TJ. Bone biology and anabolic therapies for bone: current status and future prospects. *J Bone Metab*. 2014;21(1):8–20.
42. Xie H, et al. PDGF-BB secreted by preosteoclasts induces angiogenesis during coupling with osteogenesis. *Nat Med*. 2014;20(11):1270–1278.
43. Li C, William OB, Cao X, Wan M. LRP6 in mesenchymal stem cells is required for bone formation during bone growth and bone remodeling. *Bone Res*. 2014;2(1):43–54.
44. Wang W, et al. Mesenchymal stem cells recruited by active TGFβ contribute to osteogenic vascular calcification. *Stem Cells Dev*. 2014;23(12):1392–1404.
45. Li C, et al. Disruption of LRP6 in osteoblasts blunts the bone anabolic activity of PTH. *J Bone Miner Res*. 2013;28(10):2094–2108.
46. Li H, et al. A novel microRNA targeting HDAC5 regulates osteoblast differentiation in mice and contributes to primary osteoporosis in humans. *J Clin Invest*. 2009;119(12):3666–3677.
47. Xie H, et al. Estrogen receptor α36 mediates a bone-sparing effect of 17β-estrodiol in postmenopausal women. *J Bone Miner Res*. 2011;26(1):156–168.